International Journal of Machine Tools & Manufacture 118–119 (2017) 37–48

Contents lists available at ScienceDirect

International Journal of Machine Tools & Manufacture

journal homepage: www.elsevier.com/locate/ijmactool

Modeling of the instantaneous milling force per tooth with tool run-out effect in high speed ball-end milling

Kunpeng Zhu*, Yu Zhang

Institute of Advanced Manufacturing Technology, Hefei Institutes of Physical Science, Chinese Academy of Science, Huihong Building, Changwu Middle Road 801, Changzhou 213164, Jiangsu, China

ARTICLE INFO

Keywords:
Milling force per tooth Ball-end milling Tool run-out Tool wear per tooth

ABSTRACT

In the high speed milling, the tool run-out affects the cutting force greatly and results in pre-matured tool life. To investigate this relationship, an improved instantaneous milling force per tooth is proposed, with inclusion of tool run-out effect. The un-deformed chip thickness considering tool run-out are defined and modeled, according to the geometrical relationships and axial milling ranges per tooth. Meanwhile, instead of the studying the conventional average flank wear, tool wear per tooth is studied for more sensitive correlation with force. Based on milling tests with Inconel 718, the error of the force model prediction is found less than 1% against the experimental data, and the correlation between the axial instantaneous milling force and tool wear per tooth is above 0.9. The results have shown that the proposed model can accurately describe the instantaneous force per tooth including tool run out effect, and the axial force component is a good indication of tool wear condition.

1. Introduction

High speed milling (HSM) has been one of the most important machining processes in achieving complex geometrical precision parts in aerospace, telecommunications, medical instruments and many other fields [1]. The cutting force modeling of HSM is the basis of milling mechanics and the instantaneous milling force (IMF) has been the foundation for studying the machining dynamics [2]. The IMF could not only reflect the tool conditions and energy consumption, but also be utilized for process optimization and automation [3]. In these aspects, the accurate prediction of IMF is of great theoretical and practical importance. Researchers have raised a lot of IMF models under different milling conditions. Tai and Fuh [4] presented a predictive force model for ball-end milling. With geometric derivation, the model was capable to deal with many of the process variables, such as depths of cut and in the feed-rate, and it showed a good agreement with experimental measurements. By taking account the cutter geometry, friction, and the influence of vibration, Wang et al. [5] developed a dynamic cutting force model for end-milling. The cutting edges were discretized into elements, and by summing up the cutting forces generated by each elemental edge, the IMFs could then be determined. Similar studies were reported in [6] by modeling the cutting forces based orthogonal cutting data with tool error considerations. In these studies, there were an underlying assumption that the force was proportional to the instantaneous un-deformed chip thickness (UCT). While taking account both the differential and oblique cutting mechanics, Jia et al. [7] developed an IMF model with the consideration of the workpiece material properties. The metal cutting process was taken as the linear superposition of a series of differential oblique cutting processes, and an inverse method was applied to obtain the specific coefficients thought edge elements. Under a more complicated condition, Tuysuz et al. [8] studied the cutting forces by modeling the UCT distribution, and the cutting and indentation mechanics. The distribution of UCT and geometry of indentation zone were evaluated by considering five-axis motion of the tool along the tool path. In these force models, the specific milling force coefficients (MFCs) are to be determined based on experimental data, and they are closely related to milling process parameters and hard to generalize. Mark and Schmitz [9] showed that milling process parameters such as feed per tooth, spindle speed, and radial immersion exhibited a nonlinear relationship with the specific MFCs. It was found that low feed rates, which were often recommended for hard-to-machine materials, produced disproportionately larger cutting forces per uncut chip area than high feed rates, particularly for low radial immersion milling. A comprehensive review of the work performed in the force modeling, such as empirical, mechanistic and analytical models was investigated in [10].

The model parameters, such as chip thickness, instantaneous force and coefficients, are to be determined in mechanistic force models. The

* Corresponding author.
E-mail address: zhukp@iamt.ac.cn (K. Zhu).

http://dx.doi.org/10.1016/j.ijmachtools.2017.04.001
Received 11 January 2017; Received in revised form 1 April 2017; Accepted 4 April 2017
Available online 06 April 2017
0890-6955/

Abbreviations and Nomenclature

CWE	Cutter-workpiece engagement
IMF(s)	Instantaneous milling force(s)
MFC(s)	Milling force coefficient(s)
SSP(s)	Statistical sampling period(s)
UCT	Un-deformed chip thickness
a_p	z-axial depth of milling
a_w	r-axial width of milling
b_w, b_s	Width and length of workpieces
db	Un-deformed chip width
d$\boldsymbol{F}_j$, dF_{qj}	Elemental IMFs of j-th flute in P-tra coordinate system, q=t, r, a
d$\boldsymbol{F}_{\mathbf{M}j}$, d$F_{\mathrm{M}qj}$	Elemental IMFs of j-th flute in P-tra coordinate system, q=t, r, a
dz	z-axial length of milling element
$\boldsymbol{F}_j$, F_{qj}	IMFs of j-th flute, q=x, y, z
f_z	Feed rate of the workpiece
g	Unit step function
h_j, $h_{j(\mathrm{ro})}$	UCT of j-th flute w/ & w/o tool run-out
i, j	Serial number of flutes
$\boldsymbol{K}$, K_{qc}	MFCs, q=t, r, a
N_t	Total flutes number of the cutter
n_t	Spindle speed of cutter
p_e	Total milling steps
r	r-axial radius of milling element
R	Radius of cutter flute edge
r_0	Tool run-out length
r_{max}	r-axial radius of element where z=a_p
$\boldsymbol{T}$	Transfer coefficient matrix
t	Machining time
$\overline{VB}$	Average tool wear
VB_j	Tool wear of j-th flute
z	z-coordinate of milling element
z_{ju}, z_{jd}	z-axial upper and lower boundaries of CWE
α_0	Tool run-out angle
β	Helix angle of cutter
β_c	Helix angle of cylindrical part of cutter
$\boldsymbol{\delta}$	The errors of IMFs and experimental data
$\Delta\phi$	Extra lag angle of cutter
κ	a-axial angle of CWE
ρ	Pearson correlation coefficient
$\boldsymbol{\Phi}$	Boundaries of machining areas
$\boldsymbol{\Phi}_0$, $\boldsymbol{\Phi}_1$	Central angles of machining areas w/ & w/o tool run-out
ϕ_j	r-axial angle of j-th flute of CWE
ϕ_{max}	Maximum center angle of real milling area
ϕ_p	Pitch angle
ϕ_s	Initial angle phase
ϕ_{ze}	r-axial angle of 1st flute of CWE when z=0
ψ	Lag angle of cutter
ψ_{max}	Maximum lag angle of cutter

major influencing factors to these parameters are tool run-out and cutter edge wear. The cutter track and IMF could be described more accurately by inclusion of tool run-out. Wojciechowski [11] modeled the milling displacement within length of tool run-out based on the geometric parameters of the ball-end cutter, and it shown that the milling displacement is affected greatly by the tool run-out in experiments. Hao et al. [12] set up the IMF model with tool run-out using the linear interpolation method in curved surface machining. The descrip-

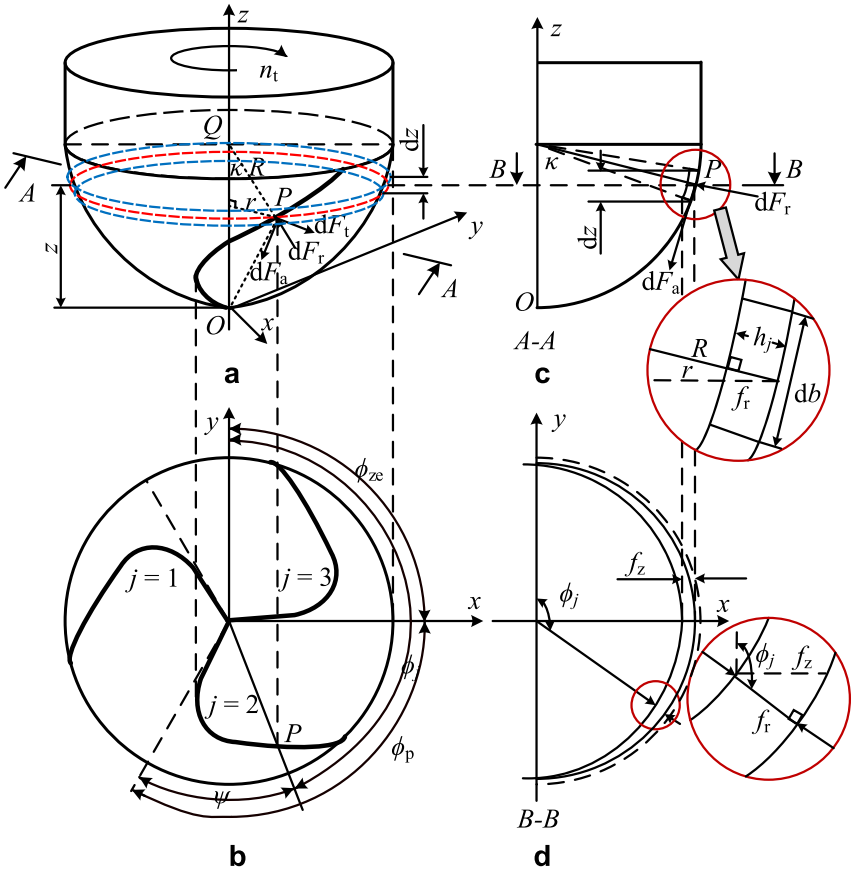

Fig. 1. Schematic diagram of a 3-flute ball nose milling cutter. (a) Flutes in front view (b) and top view. (c) Elemental chip in front view (d) and top view.

tion formulas of in and out angles in milling were determined by the iteration method, which improved the accuracy of the model, but the run-out parameters were not discussed in detail. According to a theoretical envelope model, Sun et al. [13] identified that the surface error of the workpiece was caused by the inclination angle of the main shaft, the angle and length of the tool run-out. However, the tool run-out variations were not modified accordingly in the study. Li et al. [14] proposed an approach to predict the cutting forces in five-axis milling process with a general end mill considering the tool runout effect. Based on the analytical model of cutting edge combined, the analytical rotary surface formation was derived by each cutting edge undergoing general spatial motion. In comparison with the true UCT calculated by the trochoidal tooth trajectory model, the approximation error introduced by the circular assumption is negligible while the computational efficiency improves a lot. In the ultra-precision and micro-milling, the runout effect is more significant, as it plays an important role on impacting surface quality and tool wear [15].

On the other hand, tool wear is inevitable in the milling process, and it is an important factor affecting the cutting mechanics and the workpiece quality. The tool wear lead to the increases of MFCs [16], increased the friction between the chip and the tool, and the increased instantaneous force would then accelerate tool wear [17]. As a result, the tool wear and cutting force were interacted. There were a lot of worked carried out to investigate the cutting force on tool wear mechanics and on tool wear monitoring. Kuljanic and Sortino [18] introduced tool wear indicators which could be determined by the features of cutting force signals, such as normalized cutting force and torque-force distance. Huang et al. [19] developed an approach for fault detection and diagnosis based on an observer model. A robust observer was designed by applying an uncertain linear model for describing the system. It was used as a tool wear estimator, and fault detection was carried out by using the observed variables and cutting force. Zhu et al. [20] studied the time-frequency characteristics cutting force and found the variation feature of force waveforms was good for on-line tool wear monitoring. Ibaraki and Shimizu [21] presented a long-term control scheme of cutting forces to regulate tool life in end milling. The cutting force was monitored only at every “check point” but not continuously, and resulted in a simplified force estimation scheme. The approach was claimed to have good generalization when basic assumptions were met. A comprehensive tool condition monitoring approaches based on smart spindle can be found in [22].

From the above analysis, the milling force models have been extensively studied, but the studies were most concerned with the overall milling cutting dynamics and using the average flank wear as tool wear indication. In practice, due to tool runout and other machining parameters, each tooth of the cutter has different interaction with workpiece, and the wear of each tooth is not consistent. To meet these difficulties, the instantaneous force per tooth is studied and the tool runout is considered in ball-end milling in this study. An improved cutting force model is developed to describe the cutting mechanics and the relationship between the tool wear and the cutting force per tooth. Details of the proposed model are developed in the following sections.

2. Modeling of the three dimensional instantaneous milling force per tooth

2.1. The instantaneous milling force model

This study intends to develop a general milling force model, and without loss of generality, it focuses on a 3-flute ball nose end milling cutter with constant helical lead for the convenience of discussion. This is one of the most widely applied types of cutters in high speed milling. The milling force can be modeled according to the cross-sectional area of instantaneous milling [23,24]. The main geometric parameters of the cutter edge are shown in Fig. 1. The hemispherical center of the cutter is Q, and the Cartesian coordinate system O-xyz is established with a point O, the hemisphere vertex, as its origin. The point P is on the cutter edge of the j-th (j=1, 2, ..., N_t) flute, where N_t is the total flutes number of the cutter. The flute radius is R, with $\overrightarrow{PQ}=R$ (mm) as shown in Fig. 1a. The serial numbers of flutes are set in the counter clockwise direction (Fig. 1b). The z-coordinate of point P is z ($z>0$, mm). The spindle speed n_t is set in the clockwise direction.

The neighborhood at the point P in the z-axis direction is chosen as the milling element, whose length is dz. The dynamic Cartesian coordinate system P-tra is established with the point P as its origin, and the t-, r- and a-axes are paralleled to the directions of instantaneous tangential, radial, and axial milling forces, as shown in Fig. 1a, c. According to the basic formulas of the instant rigidity forces [25,26], the elemental IMFs $\mathrm{d}\boldsymbol{F}_{\mathbf{M}j}(t, z)=(\mathrm{d}F_{tj}, \mathrm{d}F_{rj}, \mathrm{d}F_{aj})^{\mathrm{T}}$ (N) in the P-tra coordinate system of the point P are given as:

$$\boldsymbol{d}\mathbf{F}_{\mathbf{M}j}(t, z) = \mathbf{K}h_j(t, z)\boldsymbol{d}b(z) \qquad (j = 1, 2, \ldots, N_t) \tag{1}$$

where the elements in the matrix $\boldsymbol{K}=(K_{\mathrm{tc}}, K_{\mathrm{rc}}, K_{\mathrm{ac}})^{\mathrm{T}}$ (N/mm^2) are MFCs in t-, r- and a-axes directions, which can be determined by the identification method based on experimental data. The coefficients in the matrix $\boldsymbol{K}$ are related to milling parameters and the material of the workpiece and the cutter. The UCT h_j (mm) and width db (mm) of the un-deformed chip are also related to the geometrical parameters of the cutter.

Referring to the geometry of the cutter in Fig. 1c, the un-deformed chip width db in Eq. (1) is given as:

$$\boldsymbol{d}b(z) = \boldsymbol{d}z\cdot\csc\kappa(z) \tag{2}$$

where κ (deg.), $\angle OQP$ in Fig. 1c, is the a-axial angle of the cutter-workpiece engagement (CWE) of the point P, and it can be expressed as:

$$\kappa(z) = \begin{cases} \arccos(1 - z/R) & (z < R) \\ \boldsymbol{\pi}/2 & (z \geq R) \end{cases} \tag{3}$$

The elemental IMFs $\mathrm{d}\boldsymbol{F}_j(t,z)=(\mathrm{d}F_{xj}, \mathrm{d}F_{yj}, \mathrm{d}F_{zj})^{\mathrm{T}}$ (N) in the x-, y- and z-axes directions can be derived by coordinate transferring as:

$$\boldsymbol{d}\mathbf{F}_j(t, z) = \mathbf{T}\boldsymbol{d}\mathbf{F}_{\mathbf{M}j}(t, z) \tag{4}$$

where the matrix $\boldsymbol{T}$ transforms the dynamic coordinate system P-tra into the fixed coordinate system O-xyz, given as, $\mathbf{T} = \begin{pmatrix} -\cos\phi_j & -\sin\kappa\sin\phi_j & -\cos\kappa\sin\phi_j \\ \sin\phi_j & -\sin\kappa\cos\phi_j & -\cos\kappa\cos\phi_j \\ 0 & \cos\kappa & -\sin\kappa \end{pmatrix}$, where ϕ_j is the r-axial angle of the CWE.

The IMFs of each flute can be obtained by integrating the elemental IMFs of each layer along the z-axis as:

$$\mathbf{F}_j(t) = \int_{z_{jd}}^{z_{ju}} \boldsymbol{d}\mathbf{F}_j(t, z) \tag{5}$$

where the z-axial upper and lower boundaries of the CWE, $z_{j\mathrm{u}}$ and $z_{j\mathrm{d}}$ (mm), are determined by the r-axial angle ϕ_j (deg.), as shown in Fig. 1b, which are correspond to the entry and exit moments of the CWE respectively.

Based on the above formula, the overall model with milling time t (s) can be derived as a single variable of 3D dynamic IMFs of a ball nose cutter by summing up the IMFs $\boldsymbol{F}_j$ (N) of each flute. The theoretical IMFs in the x-, y- and z-axes are given as:

$$\mathbf{F}(t) = \sum_{j=1}^{N_t} \mathbf{F}_j(t) \quad (t \geq 0) \tag{6}$$

Based on Eqs. (1) and (5), it requires a specific analysis of the milling process parameters which are to be determined for the model of IMFs per tooth to be solved. The variations of the UCT h_j with tool run-out and the z-axial boundaries $[z_{j\mathrm{u}}, z_{j\mathrm{d}}]$ of the CWE with the r-axial angle ϕ_j are to be defined, which are studied in the below sections accordingly.

2.2. Determination of the un-deformed chip thickness (UCT)

When not considering the influence of physical factors, such as milling system chatter and the tool wear, the UCT h_j at milling time t in Eq. (1) can be derived similar to [27]. Based on the geometry of a ball nose milling cutter in Fig. 1c, d, when the length dz of the milling element at the point P approaches 0, h_j is given as:

$$h_j(t, z) = f_r \sin(\kappa(z)) = f_z \sin\left(\phi_j(t, z)\right)\sin(\kappa(z)) \tag{7}$$

where f_z (mm s^{-1}) is the feed rate of the workpiece. In accordance with the position angles of a milling cutter in Fig. 1b, the r-axial angle ϕ_j is given as:

$$\phi_j(t, z) = \phi_{ze}(t) - (j-1)\phi_p - \psi(z) \tag{8}$$

where ϕ_p is the pitch angle and $\phi_p=2\pi/N_t$, and ϕ_{ze} is the r-axial angle while the z-coordinate, z, of the first flute (j=1) is equal to 0. The initial angle phase ϕ_s is equal to ϕ_{ze} at the initial sampling time (t=0), and it's related to the sampling selection time merely, given as $\phi_s\in[0, \phi_p)$. ϕ_{ze} can be derived as:

$$\phi_{ze}(t) = \phi_s + 2\pi n_t t/60 \tag{9}$$

where n_t (rpm) is spindle speed of the cutter.

The $\psi(z)$ in Eq. (8) is the lag angle that is caused by the helical shape of flutes, which can be determined through the geometrical relations as:

$$\psi(z) = [z \tan(\beta(z))]/r(z) \tag{10}$$

where β is the helix angle of the cutter. According to the geometric model in Fig. 1 and Eq. (3), the r-axial radius r (mm) at point P and β are then given as:

$$\{r(z) = R \sin(\kappa(z))\beta(z) = \arctan[(r(z)\tan\beta_c)/R] \tag{11}$$

where β_c is the helix angle of cylindrical part of the cutter.

2.3. Determination of the boundaries of the cutter-workpiece engagement (CWE)

When the milling is not deep slotting, the depth a_p of milling is less than cutter radius R, and the radial width a_w of milling is not more than r. It is reasonable to assume that the point P is at flute edge which is located in the largest depth of cut, i.e., z=a_p, as shown in Fig. 2a. Based on Eq. (10), the maximum lag angle ψ_{max} and the radius r_{max} at maximum depth of milling can be derived respectively as:

$$\begin{cases}\psi_{max} = \psi(a_p) = (a_p \tan\beta_c)/R & r_{max} = r(a_p) = \sqrt{R^2 - (R-a_p)^2}\end{cases} \tag{12}$$

Without considering the feed rate f_z of the workpiece, and with the geometrical relations (Fig. 2a), the milling area can be divided into four parts: the part I of the flute entry, the part II of the complete milling, the part III of the flute exit and the part IV where the cutter isn't participating in milling. The corresponding central angles of each area can be expressed successively as:

$$\boldsymbol{\Phi}_0 = [\psi_{max} \quad \pi - \psi_{max} \quad \psi_{max} \quad \pi - \psi_{max}]^T \tag{13}$$

The counter clockwise direction is identified as the positive direction of extra lag angle $\Delta\phi$, which is related to f_z, as shown in Fig. 2c. By considering f_z, the $\Delta\phi$ is then given as:

$$\Delta\phi = \arcsin(f_z/r_{max}) \tag{14}$$

For each sub-milling area, considering the effect of f_z, the corresponding center angles of the four parts can be determined respectively as:

$$\boldsymbol{\Phi}_1 = \boldsymbol{\Phi}_0 + \frac{N_t\phi_{max}\Delta\phi}{2\pi}[-1 \quad 0 \quad 1 \quad 0]^T \tag{15}$$

In the actual milling process, if the radial width a_w of milling is less than the radius at the maximum depth of milling r_{max}, as shown in Fig. 2b, the maximum center angle ϕ_{max} of real milling area is then given as:

$$\phi_{max} = \arccos[(r_{max} - a_w)/r_{max}] \tag{16}$$

Generally, the equality holds with $\psi_{max}+\phi_{max}=2\pi$. The unit step function g, whose value depends on the relations between the maximum center angle ϕ_{max} of real milling area and the maximum lag angle ψ_{max}, is applied to characterize the discontinuous milling process. The function g can be expressed as:

$$g = \begin{cases}1 & (\psi_{max} \geq \phi_{max}) \\ 0 & (\psi_{max} < \phi_{max})\end{cases} \tag{17}$$

It is noted that the projection of the milling direction in the x-axis is the same as the feed direction of the workpiece in the part I, II and III areas, i.e., the extra lag angle $\Delta\phi$ is positive, as shown in the below figure in Fig. 2c. The central angles in Eqs. (13) and (15) can be modified as:

$$\begin{cases}\boldsymbol{\Phi}_0 = [\min(\psi_{max}, \phi_{max}) \quad |\psi_{max} - \phi_{max}| \quad \min(\psi_{max}, \phi_{max}) \quad 2\pi - \phi_{max} - \psi_{max}]^T \\ \boldsymbol{\Phi}_1 = \boldsymbol{\Phi}_0 + \Delta\phi\left[\frac{\min(\psi_{max}, \phi_{max})}{\psi_{max}+\phi_{max}} \quad \frac{|\psi_{max} - \phi_{max}|}{\psi_{max}+\phi_{max}} \quad \frac{\min(\psi_{max}, \phi_{max})}{\psi_{max}+\phi_{max}} \quad -1\right]^T\end{cases} \tag{18}$$

The boundary can be illustrated by studying the column vector $\boldsymbol{\Phi}$, with its i-th element represented as $\boldsymbol{\Phi}(i)$. The boundaries of four areas are calculated respectively as:

$$\boldsymbol{\Phi}(i) = \sum_{i_0=1}^{i} \boldsymbol{\Phi}_1(i_0) \quad (i_0 \leq i \leq 4;\ i,\ i_0 \in N^+) \tag{19}$$

The z-axial milling boundaries of the CWE of the j-th flute at time t are $[z_{ju}, z_{jd}]$. The point P is selected on the y-axis at the initial moment of milling. The position angle φ_j, which is a function in a period of the

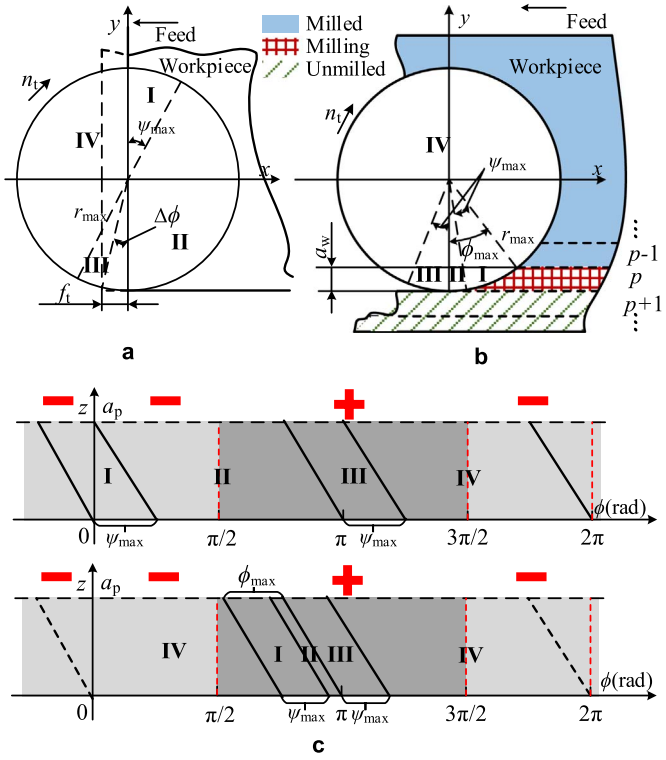

Fig. 2. Position angles. (a) the CWE when a_w=2r_{max} and (b) $a_w < r_{max}$. (c) Expansion diagrams of position angles.

Table 1
The analysis results of the CWE.

The position angle φ_j	z-axial boundaries $[z_{ju}, z_{jd}]$
$[0, \Phi(1))$	$z_{jd}(t) = 0;\ \ z_{ju}(t) = R\varphi_j \frac{\Phi_0(1)}{\Phi_1(1)} \cot\beta_c$
$[\Phi(1), \Phi(2))$	$\begin{cases} z_{jd}(t) = gR\left(\varphi_j - \Phi(1)\right)\frac{\Phi_0(3)}{\Phi_1(3)} \cot\beta_c \\ z_{ju}(t) = (1-g)a_p + gR\varphi_j \frac{\Phi_0(1)}{\Phi_1(1)} \cot\beta_c \end{cases}$
$[\Phi(2), \Phi(3))$	$\begin{cases} z_{jd}(t) = R\left[\varphi_j - (1-g)\Phi(2) - g\Phi(1)\right]\frac{\Phi_0(3)}{\Phi_1(3)} \cot\beta_c \\ z_{ju}(t) = a_p \end{cases}$
$[\Phi(3), \Phi(4))$	$z_{jd}(t) = 0;\ \ z_{ju}(t) = 0$

time variable t, can be expressed as $\varphi_j(t) = \phi_j(t, 0) - 2k\pi$. For any $t > 0$, there exists exactly one $k \in N$, which leads to $\varphi_j \in [0, 2\pi)$. Table 1 shows the z-axial boundaries $[z_{ju}, z_{jd}]$ in each milling areas. According to the analysis of the z-axial boundaries $[z_{ju}, z_{jd}]$, the IMFs $\boldsymbol{F}_j$ per tooth in Eq. (5) can be calculated.

2.4. Modeling of the un-deformed chip thickness considering tool run-out

Since the tool run-out changes the state of the CWE, the UCT h_j needs to be modified based on the shape and the parameters of the tool run-out, which results in periodic fluctuating milling forces [28]. At the same time, the position error on the surface of the workpiece is formed, and the surface roughness and milling stability are affected [29]. The tool run-out is characterized by the run-out length r_0 and the run-out angle α_0 [30,31], and the height of cutters is expressed as a_h, as shown in Fig. 3a.

Milling processes of two neighboring flutes of a ball nose end cutter in the same z-axial depth of milling are shown in Fig. 3b without considering the tool run-out. The point Q_j and Q'_j are the centers of the current flute edge circles in the xOy plane without/with considering the tool run-out. The run-out length $r_0 = \overline{Q_jQ'_j}$, and the run-out angle α_0 is the angle between r_0 and the tangent line of the first flute edge, as shown in Fig. 3c. Similarly, the point Q_i and Q'_i are the centers of the previous flute edge circles in the xOy plane without/with considering the tool run-out, where $i = 1, 2, \ldots, N_t$. According to the series of flute numbers in Fig. 1b, the relation of serial numbers of the current and previous flutes is given as:

$$i = j - 1 + N_t\lfloor (N_t + 1 - j)/N_t \rfloor \quad (j = 1, 2, \ldots, N_t) \tag{20}$$

where the integral symbol $\lfloor x \rfloor$ represents the maximum integer which is not more than the real variable x.

Under this condition, the variation of the UCT h_j in milling is shown in Fig. 3d. The Eq. (6) about h_j is then modified accordingly as:

$$h_{j(ro)}(t, z) = \max(0, h_j + \Delta h_j - \Delta h_i) \tag{21}$$

Table 2
Parameters of experimental setup.

Parameters	Specifications or values
Material of workpieces	Inconel 718
Hardness of workpieces (HRC)	45
Size of workpieces $b_s \times b_w$ (mm)	112.5×40
Material of cutters	Tungsten carbide
Type of cutters	3-flute ball nose
Types of milling	Half-immersion, slotting
Measuring instrument	Kistler 9119AA2
Sampling frequency f (kHz)	50
Milling steps p_e	320
height of cutters a_h (mm)	78

where Δh_j and Δh_i are the extra UCTs that are caused by the tool run-out of the current and previous flutes respectively. They are expressed as:

$$\Delta h_k(t, z) = r_0 \sin(\kappa(z))\cos\left[\alpha_0 + \psi(z) + (k-1)\phi_p\right] \quad (k = i, j) \tag{22}$$

According to above analysis of the z-axial boundaries $[z_{ju}, z_{jd}]$ and the UCT $h_{j(ro)}$ in Table 1 and Eq. (21), the dynamic milling force per tooth in Eq. (5) can be determined finally. Based on the Experimental data and the theoretical milling force in Eq. (6), the overall approach is tested and validated in the Section 3.

3. Experimental validation

3.1. Experimental setup

As in Section 2, 3-flute ball nose end milling cutters are chosen in the experiments to validate the developed approach. The material of workpiece is Inconel 718, the Ni-based superalloy. This material has good physical properties in the high temperature environment, such as the high strength, and it's used in the fields of aerospace, biomedical and electronic devices etc. However, it has issues such as high cutting force, high cutting temperature and that the cutter is easy to be worn in high speed milling, which will lead to low quality or even defect product. It is necessary to investigate the cutting force and tool conditions so as to achieve optimized milling process. The milling parameters and experimental conditions of the workpiece cutter system and the sampling equipment are shown in Table 2. The IMFs are measured by the Kistler 9119AA2 dynamometer, and the sampling frequency is 50 kHz. The tool run-out is experimentally measured with a dial gauge indicator when the spindle has rotated 360°.

The work platform is arranged on the high speed machining center MIKRON HSM600U, as shown in Fig. 4a. Referring to the milling parameters in Fig. 4b, the parameters of the depths of cut, the feed rates of workpieces and the spindle speeds etc. are listed in Table 3. All the tests are repeated three times to eliminate the uncertainties. The

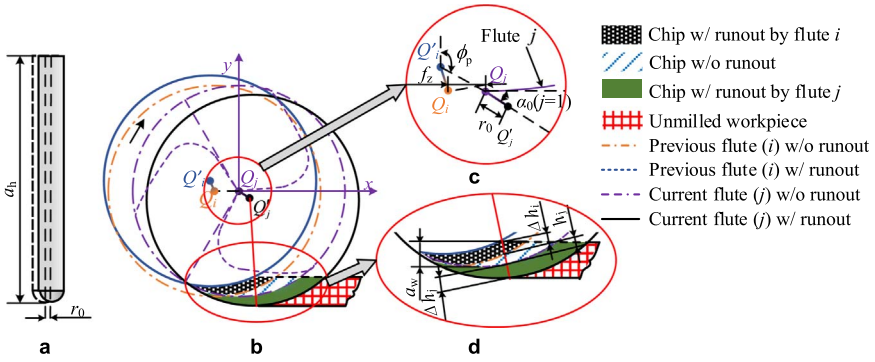

Fig. 3. Effect of the tool run-out. (a) Type of run-out. (b) Modeling of UCT. (c) Run-out parameters. (d) Extra UCT.

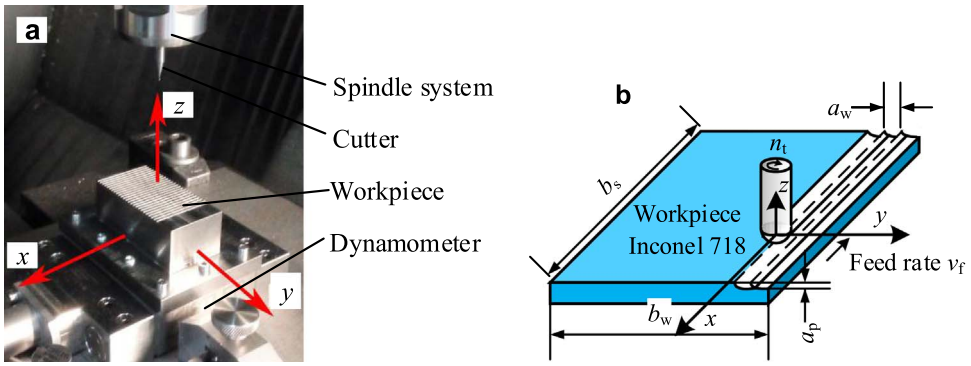

Fig. 4. Experimental setup. (a) Platform and (b) milling parameters.

Table 3
Machining conditions of experiments.

Test No.	a_p (mm)	a_w (mm)	f_z (μm/tooth)	n_t (rpm)	Types of milling
1	0.2	1.960	30	8000	Slotting
2	0.2	1.960	10	10000	Slotting
3	0.2	1.960	30	10000	Slotting
4	0.15	1.706	50	10000	Slotting
5	0.2	1.960	50	10000	Slotting
6	0.25	2.179	50	10000	Slotting
7	0.2	1.960	30	20000	Slotting
8	0.2	1.960	30	30000	Slotting
9	0.15	0.075	50	10000	Half immersion
10	0.2	0.100	50	10000	Half immersion
11	0.25	0.125	50	10000	Half immersion
12	0.15	1.874	10	10000	Slotting
13	0.25	2.400	30	8000	Slotting
14	0.25	2.400	10	10000	Slotting
15	0.25	2.400	30	10000	Slotting
16	0.2	2.154	50	10000	Slotting
17	0.25	2.400	50	10000	Slotting
18	0.3	2.615	50	10000	Slotting
19	0.25	2.400	30	20000	Slotting
20	0.25	2.400	30	30000	Slotting
21	0.2	0.100	50	10000	Half immersion
22	0.25	0.125	50	10000	Half immersion
23	0.3	0.150	50	10000	Half immersion

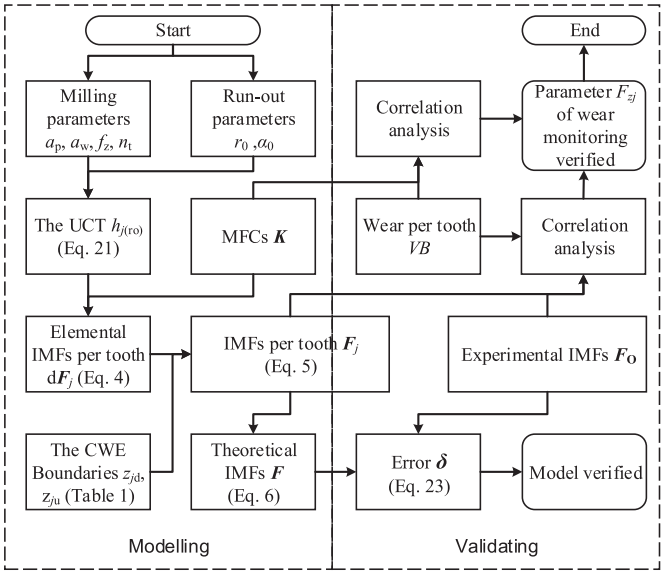

Fig. 5. Methodology flow chart of the theoretical model and experimental verification of milling force.

diameters of ball nose end milling cutters are 5 mm (test 1–11) and 6 mm (tests 12–23). Two types of milling are half-immersion and slotting, which are designed in multi groups of experiments. The cutter completes milling the workpiece surface with the spindle speed n_t in each group of experiments, and the total milling steps is p_e. The rectangular size of the workpiece surface is $b_w \times b_s$, and the total stroke length of the cutter is $p_e \times b_s$ in each group of experiments.

Appropriate parameters of milling and run-out are selected for validation of the theoretical model combining with calculation and experimental milling forces. After calculating the UCT $h_{j(ro)}$, milling force $\boldsymbol{F}_j$ and $\boldsymbol{F}$, the error $\boldsymbol{\delta}$ that is used to optimize parameters values is obtained. Correlations of milling force $\boldsymbol{F}_j$ and wear VB_j per tooth are analyzed to determine the optimal wear monitoring parameter. The overall methodology of theoretical model and experimental verification of milling force is shown in Fig. 5.

3.2. Validation of the developed milling force model

Based on empirical studies, the wear curves of each flute edge in milling shows that the tool wear increment is rather small in the steady state period of the abrasive wear, and the wear shows significant difference only after a certain long cutting stroke [32]. Therefore, the stable periods of time before each 10 steps in every group of experiments are chosen as the statistical sampling periods (SSPs). Based on the experimental data, the algorithms of milling force model are implemented to determine the run-out parameters r_0 and α_0 in each experiment, calculate and sum up the IMFs $\boldsymbol{F}$ of each layer along the z-axial direction in real-time for each step, in which the run-out parameters r_0 and α_0 are increased by Δr and $\Delta\alpha$ respectively. It obtains the optimal solution by minimizing the average error between the experimental milling force $\boldsymbol{F}_O$ and the model's. According to the theoretical model and experimental data, the flow chart of the modeling algorithm is shown in detail in Fig. 6.

The exemplary results are illustrated with the test 22 in Table 3. The stable periods in 0.02 s before the end of milling in the 10th and 110th steps are selected as the SSPs. Milling forces F_x and F_y in each steps with time t are shown in Fig. 7. The prediction amplitudes and means of milling forces are in good agreement with the experimental data in the x-axial direction. The amplitude and frequency variations increase with the milling time, which is affected by the tool wear. As shown in Fig. 7, there are three main peaks in one period on the theoretical milling force curves, which correspond to the time when flutes of the cutter are cutting the workpiece respectively. Theoretical milling force are related to the tool run-out parameters.

Amplitude frequency characteristic curves of milling forces obtained from both the experiments and the theoretical model are given in Fig. 8. The larger amplitudes are concentrated in the low frequency region mainly in the initial milling stage, and the theoretical model can accurately describe the responses of milling force in the high amplitude and low frequency region. Since the CWE hasn't reached the stable

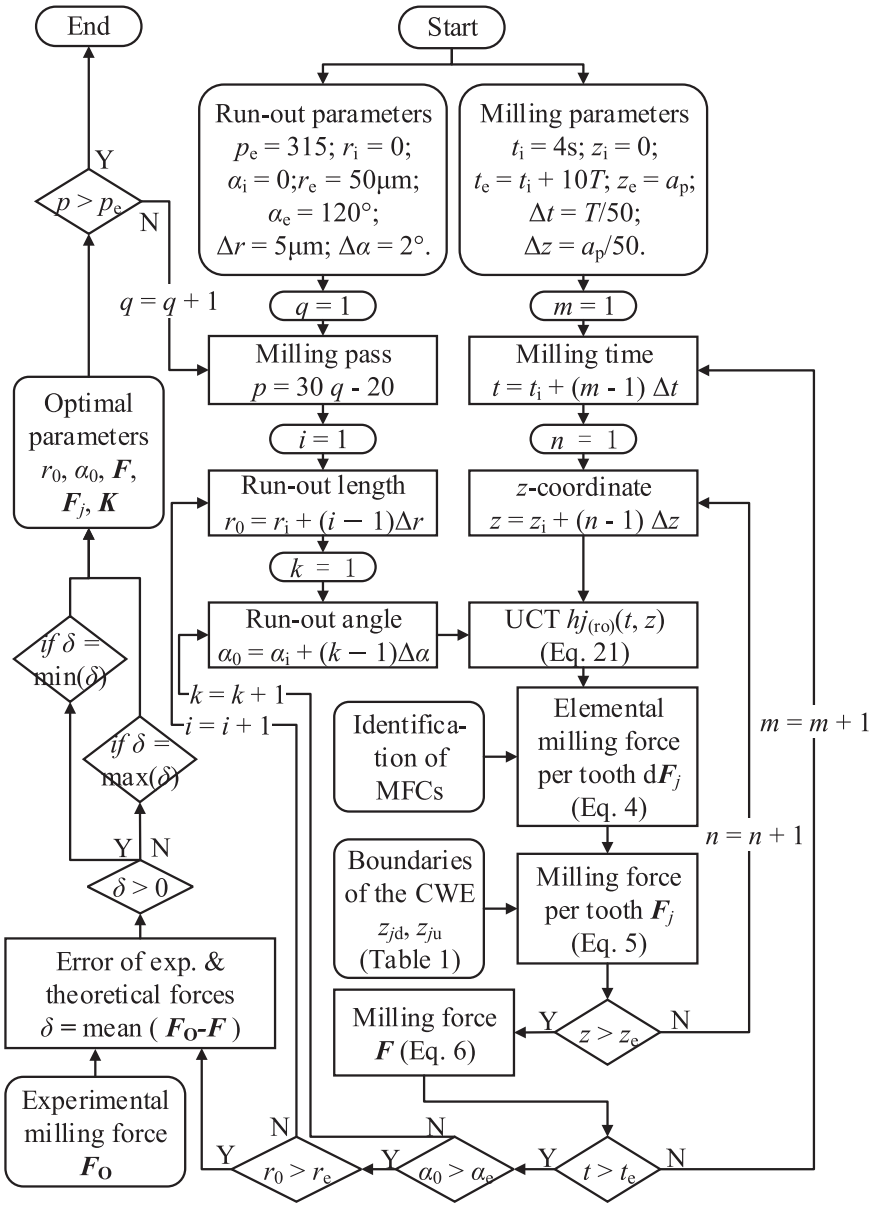

Fig. 6. The flow chart of instantaneous milling for modeling.

state in the initial milling stage, and the cutter is in the period of running-in wear, some high frequency and low amplitude interfering signals are generated in this stage, which is more obvious in the y-axial direction as shown in figures in the right column of Fig. 8. With the milling progressing, the cutter is in the adhesive wear stage and the wear is slowly increased after the initial stage before it becomes severe. As shown in the single-sided amplitude spectrum in the 11th SSP, the maximum amplitude appears in the middle frequency region, and the interfering signals decreased significantly. Milling force spectrums of the theoretical model agree with the experimental data highly. As the noise interference is not included in the theoretical model, the response amplitudes of IMFs in the model are larger than those of the experimental data.

3.3. The tool run-out and instantaneous milling force

The tool run-out parameters are determined according to the proposed model, and an example is shown in Fig. 9. Points in negative and positive approximate lines are obtained by the judgment condition, errors $\boldsymbol{\delta} > 0$, in algorithms respectively, as shown in Fig. 6. The errors $\boldsymbol{\delta}$ between the average theoretical instantaneous milling force (IMF) $\boldsymbol{F}$ and the experimental measurement $\boldsymbol{F_O}$ are given as:

$$\boldsymbol{\delta} = (\mathbf{F} - \mathbf{F_O})/\mathbf{F_O} \tag{23}$$

As can be seen, the run-out length r_0 and angle α_0 are increasing in the initial milling stage, and then become relatively stable after some time. As each experiment is carried according to the same setup, so the tool run-out characteristics are mainly related to the tool wear. The increase of tool wear leads to the larger tool run-out, and the increases of run-out will then worsen the tool wear condition. The precision and quality of the workpiece is affected seriously by the interaction of the tool run-out and wear as a result.

Fig. 10a shows that errors $\boldsymbol{\delta}$ are less than 1% in each milling process. This is mainly due to the online updating of parameters of milling and run-out in algorithms in Fig. 6, which would improve the accuracy of the force prediction largely. The characteristics of milling force $\boldsymbol{F}$ are shown in Fig. 10b, which in the x-, y- and z-axes increase with the milling time. There are two outlier regions in the experimental F_x due to data acquisition errors, which are eliminated in the analysis. The largest increment of $\boldsymbol{F}$ is in the x-axis, and it is smaller in the feed

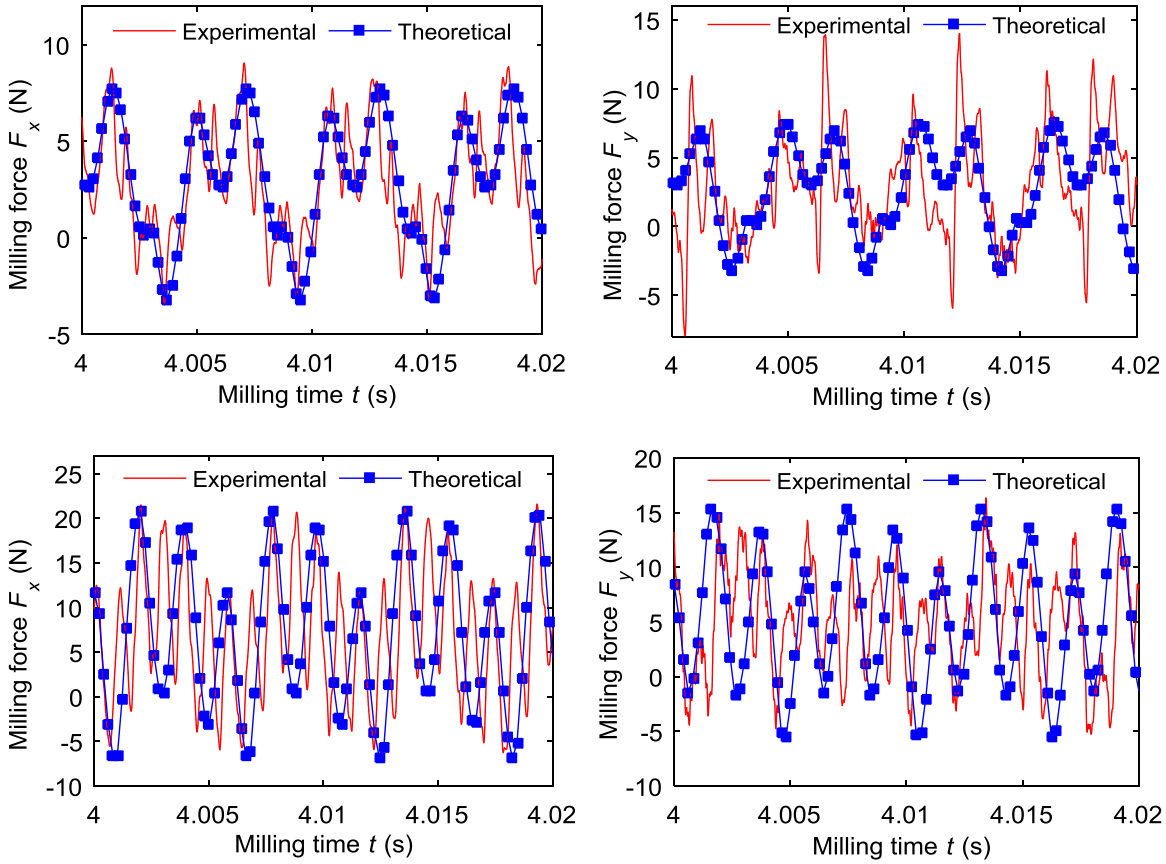

Fig. 7. Theoretical and experimental IMFs in feed (x-axial) and normal (y-axial) directions in the 1st and 11th SSPs.

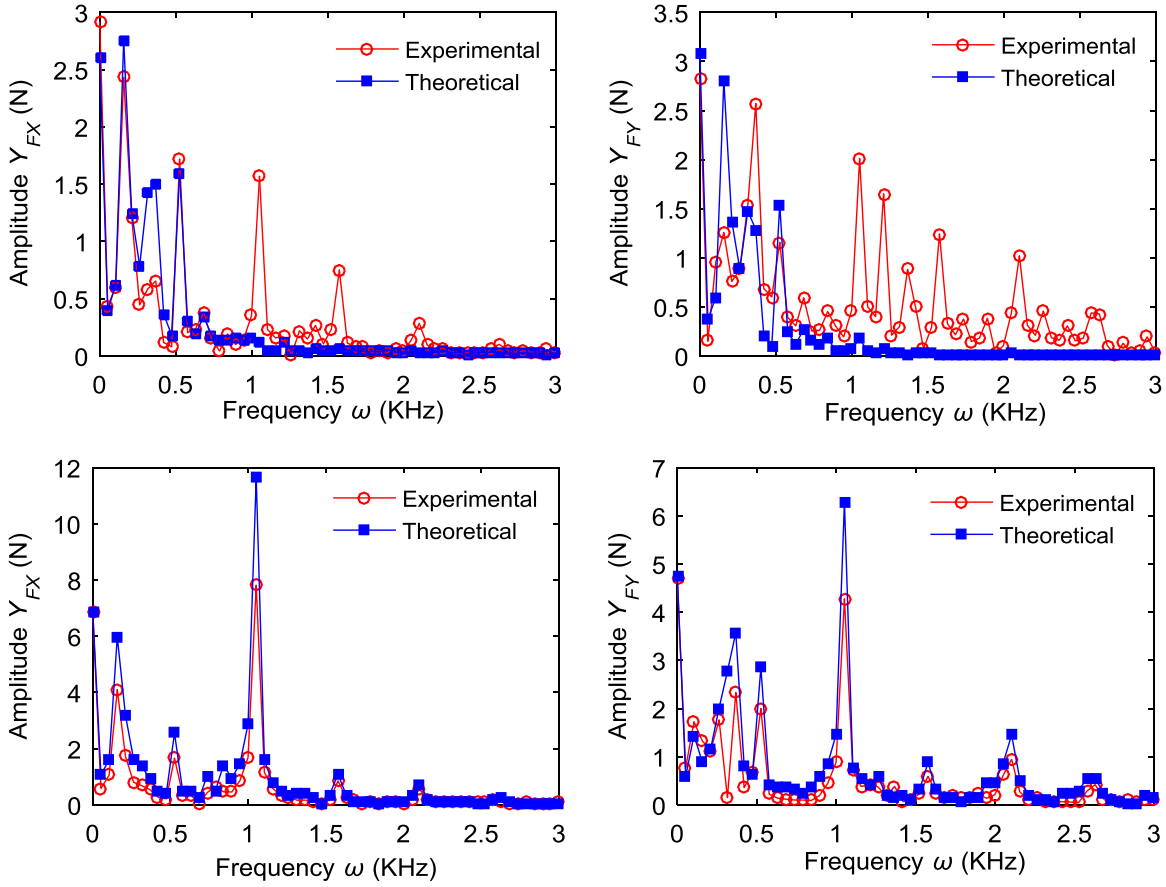

Fig. 8. Spectrums of theoretical and experimental IMFs in feed (x-axial) and normal (y-axial) directions in the 1st and 11th SSPs.

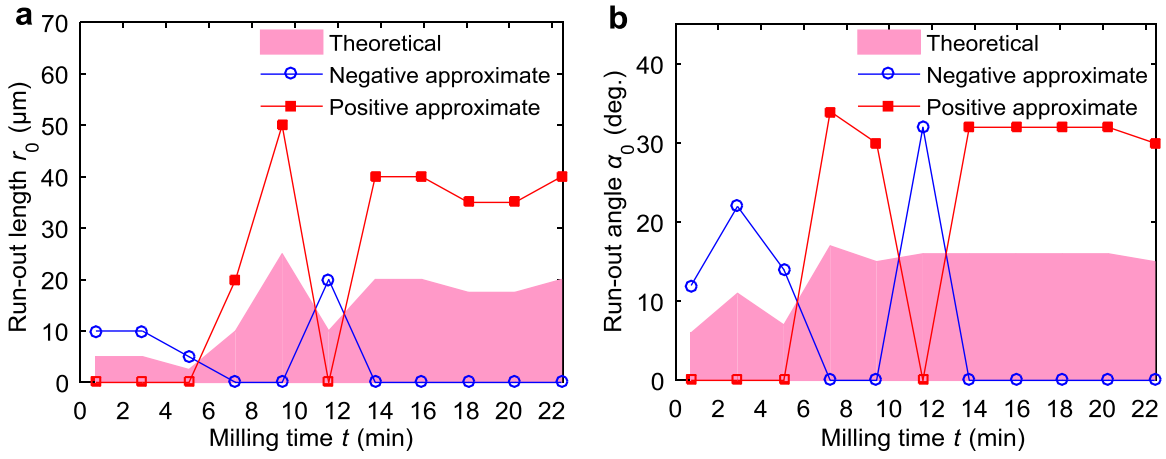

Fig. 9. Parameters of the tool run-out. (a) Run-out lengths r_0 and (b) angles α_0.

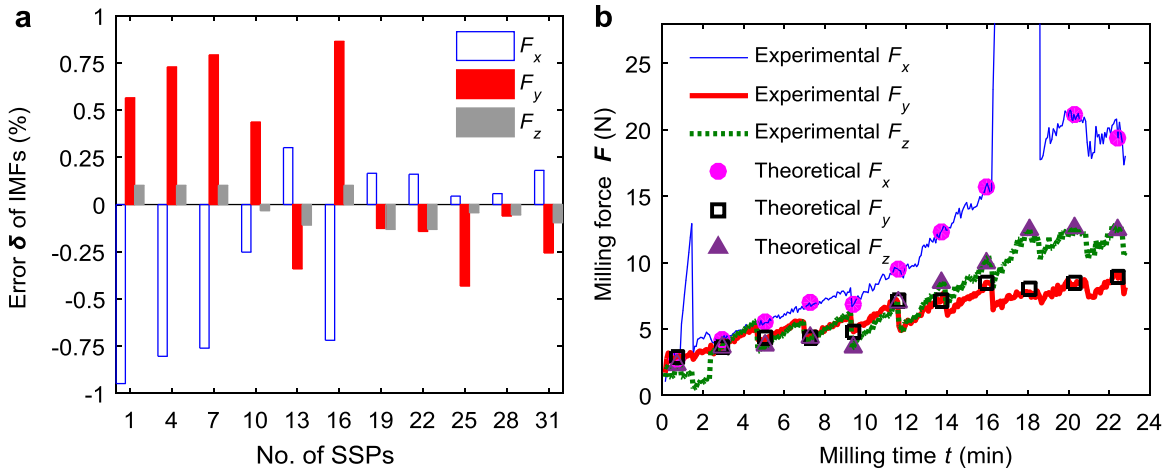

Fig. 10. Results of test 22. (a) The errors of force prediction (b) average theoretical and experimental force.

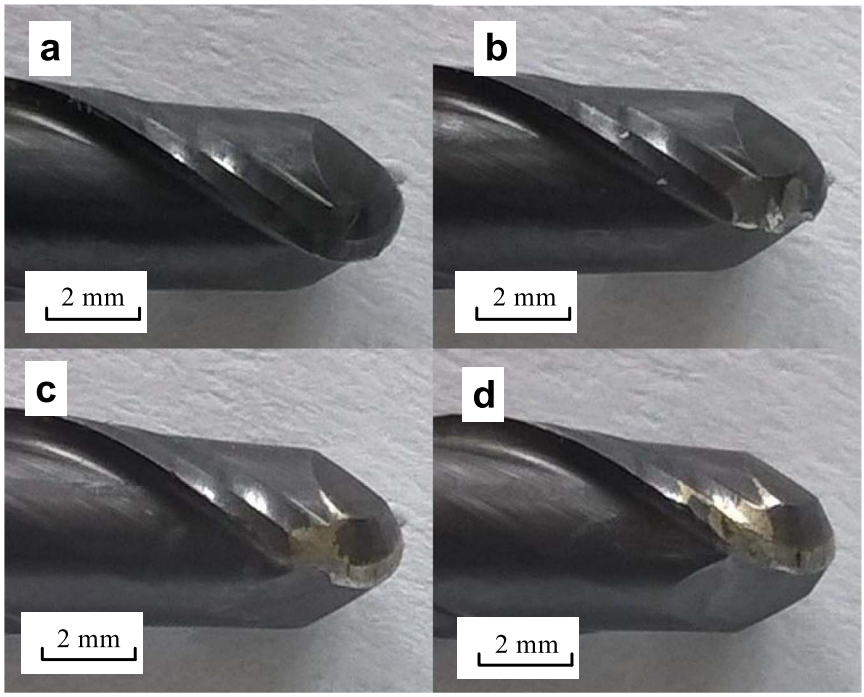

Fig. 11. Tool wear when (a) in pre-experiment, (b) in 6th, (c) 19th and (d) 31st SSPs.

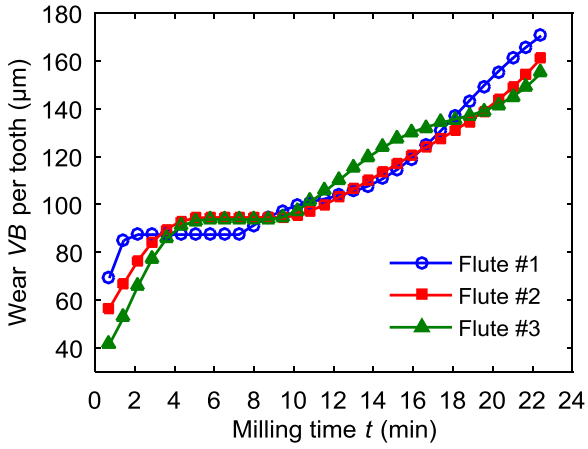

Fig. 12. Tool wear *VB* per tooth in test 22.

and *y*-axis directions. Since the tool wear is severe in the later period of milling, and there is a larger vibration effect on the cutter in z-axis, which leads to the significant increase of force in this direction.

It will be seen from the analysis that the tool wear is the main factor causing the increasing of the tool run-out parameters and the instantaneous force in milling, which affects the quality of milling. So it has an important theoretical significance and value in engineering to analyze and predict the tool wear.

3.4. The tool wear per tooth and force coefficients

Due to tool runout effect, each tooth of the cutter has different interaction with workpiece, and the wear of each tooth is not consistent. The tool wear per tooth and it correlation to the instantaneous force per tooth are studied to overcome this problem and to improve the accuracy of the correlation analysis. The process of the tool wear is shown in Fig. 11 in experiments. The tool wear has been evident in the 19th statistical sampling period (SSP), and the tool wear is severe in the 31st SSP at the end of experiments that shown in Fig. 11d. The tool wear per tooth are measured with a three-coordinate measuring machine, equipped with an industrial camera, a light source and a telecentric lens. To ensure the consistency in the whole machining process, each tooth was marked before the measurement. The tool flank wear per tooth is then obtained by counting the pixels of the wear length in the full tool image, which is captured by an industrial camera with 2 Megapixels. Tool wear curves of the experimental data are shown in Fig. 12. Each wear curve of the cutter's *j*-th flute is the anti-S shape and the trend is consistent with the typical tool wear curve in the metal cutting process [33]. The flank wearing process could roughly be divided into three regions. In the initial stage, the edge of the fresh tool is worn fast when the cutting starts, and this is followed by a gradual, approximately linear adhesive tool wear development area with milling process progressing. At the end of this progressive stage the wear land reaches a critical point and the flank wear increases exponentially or even leads to tool break. The tool must be replaced before reaching the critical limit to avoid tool failure. The tool wear monitoring is analyzed primarily by studying the instantaneous milling force and its variation features.

Based on milling force $\boldsymbol{F_O}$ in *x*-, *y*- and *z*-axes obtained from experiments, the force coefficients $\boldsymbol{K}$ are obtained by a fast calibration algorithm for identification of $\boldsymbol{K}$ that is proposed by Budak et al. [23,34]. The absolute values of $\boldsymbol{K}$ in the t-, r- and a-axes increase with milling time *t*.

According to curves of $\boldsymbol{K}$ and the average tool wear $\overline{\mathrm{VB}}$ in Fig. 13a, compared to K_{tc} and K_{rc} in t- and r-axes, the change of the a-axial K_{ac} in experiments is 3.01 and 5.89 times of the other two's, respectively. It shows that the a-axial K_{ac} is most sensitive to the change of $\overline{\mathrm{VB}}$ based on correlation analysis. The correlation coefficients ρ and *p*-values *P* of bilateral significance level α=95% in two-tailed tests of $\boldsymbol{K}$ and $\overline{\mathrm{VB}}$ are given as:

$$\{\rho(\mathbf{K}, \overline{VB}) = [\mathrm{cov}(\mathbf{K}, \overline{VB})]/(\sigma_{\mathbf{K}}\sigma_{\overline{VB}})P(\mathbf{K}, \overline{VB}) = 2\min\{\Pr(\rho \le 1 - \alpha/2|H)\} \tag{24}$$

where the covariance $\mathrm{cov}(\boldsymbol{K}, \overline{\mathrm{VB}})=\mathrm{E}[(\boldsymbol{K}-\mathrm{E}(\boldsymbol{K}))\cdot(\overline{\mathrm{VB}}-\mathrm{E}(\overline{\mathrm{VB}}))]$. E is the expectation of variables, and σ is the standard deviation of variables. Pr is the conditional probability of correlation coefficients ρ, which follows the Student t-distribution in the statistical hypothesis test *H*, given as [35]:

$$\{H_0: \rho = 0 H_i: \rho \ne 0 \tag{25}$$

where the null hypothesis H_0 indicates that there are no linear correlations of variables $\boldsymbol{K}$ and $\overline{\mathrm{VB}}$. Hypothesis H_1 refers to that there are linear correlations, whose degree is represented by correlation coefficients ρ, $\rho\in[-1, 1]$. The null hypothesis H_0 is rejected explicitly when *p*-values $P<0.01$, that is, correlations of $\boldsymbol{K}$ and $\overline{\mathrm{VB}}$ are significant.

The correlation coefficients with Eq. (24) are shown in Fig. 13b. As can be observed, the correlation coefficients ρ of $\boldsymbol{K}$ and the tool wear VB_j of the *j*-th flute in the t-, r- and a-axes are all above 0.8, and the correlation coefficients ρ of K_{ac} and VB_j of all three flutes are about 0.95. The *p*-values of bilateral significance levels are far less than 1%, which indicates a significant correlation between K_{ac} and VB_j.

By studying the correlation of the instantaneous milling force and the tool wear, it can be found that the dynamics of IMFs, especially the component in *z*-axis, reflect the progressing of tool wear per tooth. As

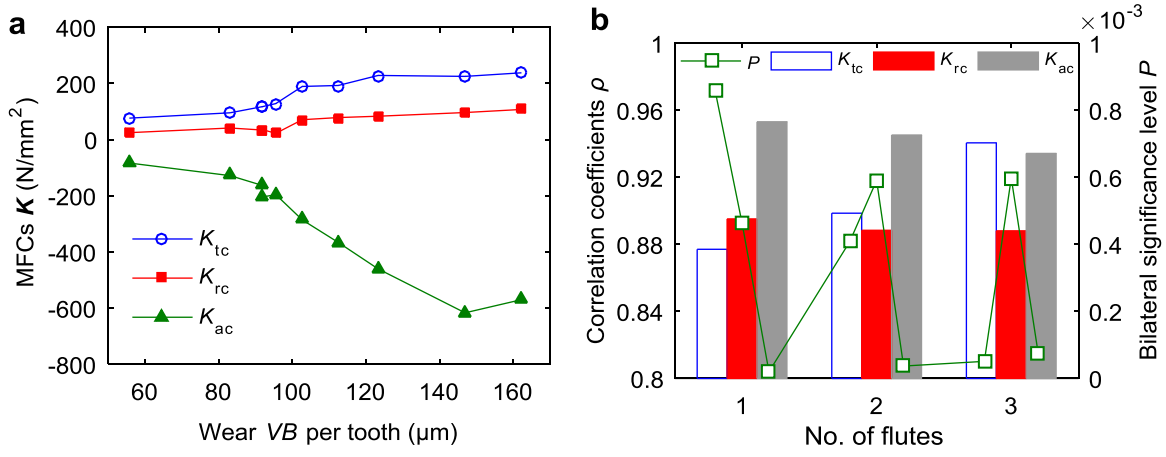

Fig. 13. (a) Relations and (b) correlations of MFCs $\boldsymbol{K}$ and tool wear *VB* per tooth.

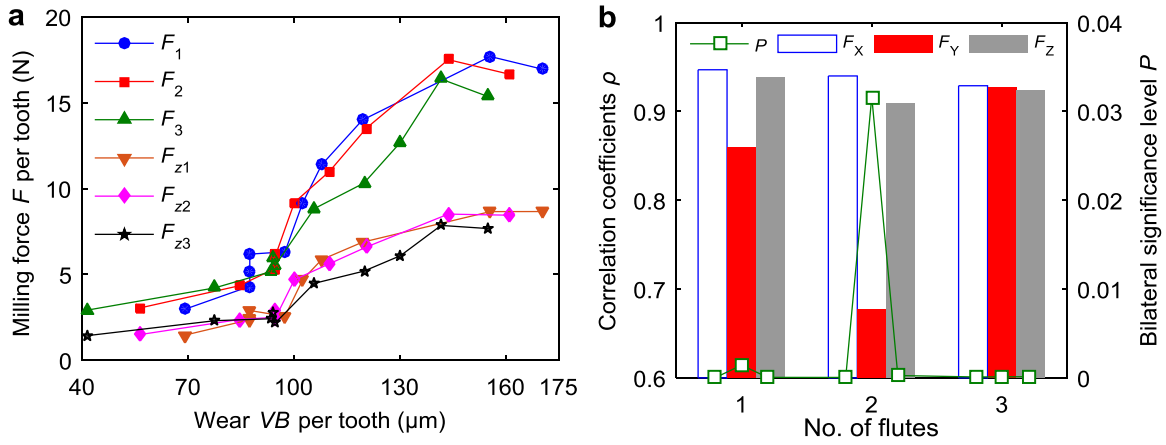

Fig. 14. (a) Relations and (b) correlations of IMFs $\boldsymbol{F}_j$ and tool wear *VB* per tooth.

an example, according to the algorithms flow chart in Fig. 6 and the resultant force in Eq. (6), the curves of the resultant forces F_1, F_2 and F_3 per tooth and the tool wear per tooth are shown in Fig. 14a. The variation tendency of F_1, F_2 and F_3 are the same generally, and the differences among the flutes in same milling time are mainly due to the tool run-out effect, which leads to different chip thickness and cutting force as a result. The Pearson correlation coefficients ρ of milling force $\boldsymbol{F}_{zj}$ in *z*-axis and VB_j are above 0.9, as shown in Fig. 14b. The *p*-values of bilateral significance levels are far less than 1%, which indicates that there is a significant correlation between $\boldsymbol{F}_{zj}$ and VB_j. Milling force $\boldsymbol{F}_{xj}$ in *x*-axis is influenced by the feed rate and the material of workpieces, while milling force $\boldsymbol{F}_{zj}$ in *z*-axis is most sensitive to the tool wear per tooth. As a result, as shown in Fig. 14, the tool wear can be monitored by studying the dynamic features of $\boldsymbol{F}_{zj}$ in real time.

4. Conclusions

This study develops a model of instantaneous cutting force per tooth with inclusion of tool run-out effect, and it is validated with high speed ball nose milling experiments under varied working conditions. In this approach, the milling forces are elaborated and modeled on each tool tooth according to the instantaneous geometric relationship and the explicitly determined tool-workpiece engagements. With the inclusion of tool run-out effect, the improved chip thickness model could reflect the real cutting dynamics and tool wear per tooth conditions accurately. The results of each milling pass have shown that the maximum error of the average predicted milling forces against with the experimental data is less than 1%. It is found that the instantaneous milling forces and the tool wear per tooth are more closely correlated when considering the tool run-out effect. The results also indicate that the resultant force in the *z*-axis direction is sensitive to the tool wear per tooth, with correlation coefficient above 0.9. In this aspect, in the future study, the feedback of the instantaneous axial resultant force would be further investigated for tool wear monitoring and for adaptive machining process control.

Acknowledgements

This project is supported by the CAS 100 Talents Program, Chinese Academy of Sciences, and the National Natural Science Foundation of China (Grant No. 51475443).

References

[1] R. M'Saoubi, D. Axinte, S.L. Soo, C. Nobel, H. Attia, G. Kappmeyer, E. Serafettin, W.M. Sim, High performance cutting of advanced aerospace alloys and composite materials, CIRP Ann. – Manuf. Technol. 64 (2) (2015) 557–580.
[2] E. Budak, Analytical models for high performance milling, part I: cutting forces, structural deformations and tolerance integrity, Int. J. Mach. Tools Manuf. 46 (12–13) (2006) 1478–1488.
[3] D. Zhu, X. Zhang, H. Ding, Tool wear characteristics in machining of nickel-based superalloys, Int. J. Mach. Tools Manuf. 64 (1) (2013) 60–77.
[4] C.C. Tai, K.H. Fuh, The prediction of cutting forces in the ball-end milling process, J. Mater. Process. Technol. 54 (1) (1995) 286–301.
[5] S.M. Wang, C.H. Chiou, Y.M. Cheng, An improved dynamic cutting force model for end-milling process, J. Mater. Process. Technol. 148 (3) (2004) 317–327.
[6] M. Svahn, C. Andersson, L. Vedmar, Prediction and experimental verification of the cutting forces in gear form milling, Int. J. Adv. Manuf. Technol. 82 (1) (2016) 111–121.
[7] Z.Y. Jia, J. Ge, J.W. Ma, Y.Y. Gao, Z. Liu, A new cutting force prediction method in ball-end milling based on material properties for difficult-to-machine materials, Int. J. Adv. Manuf. Technol. 86 (9) (2016) 2807–2822.
[8] O. Tuysuz, Y. Altintas, H.Y. Feng, Prediction of cutting forces in three and five-axis ball-end milling with tool indentation effect, Int. J. Mach. Tools Manuf. 66 (2) (2013) 66–81.
[9] M.A. Rubeo, T.L. Schmitz, Mechanistic force model coefficients: a comparison of linear regression and nonlinear optimization, Precis. Eng. 45 (2016) 311–321.
[10] D. Germain, G. Fromentin, G. Poulachon, S. Bissey-Breton, From large-scale to micromachining: a review of force prediction models, J. Manuf. Process. 15 (3) (2013) 389–401.
[11] S. Wojciechowski, The estimation of cutting forces and specific force coefficients during finishing ball end milling of inclined surfaces, Int. J. Mach. Tools Manuf. 89 (2014) 110–123.
[12] H. Hao, B. Wang, W. Tang, Prediction of instantaneous milling force taking runout into account in peripheral milling of curved surface, Int. J. Adv. Manuf. Technol. 79 (1) (2015) 49–56.
[13] Y. Sun, Q. Guo, Analytical modeling and simulation of the envelope surface in five-axis flank milling with cutter runout, ASME J. Manuf. Sci. Eng. 134 (2) (2012) 160–165.
[14] Z.L. Li, J.B. Niu, X.Z. Wang, L.M. Zhu, Mechanistic modeling of five-axis machining with a general end mill considering cutter runout, Int. J. Mach. Tools Manuf. 96 (9) (2015) 67–79.
[15] G. Li, D. Qu, W.W. Feng, B. Wang, N. Li, Modeling and experimental study on the force of micro-milling titanium alloy based on tool runout, Int. J. Adv. Manuf. Technol. 87 (1) (2016) 1193–1202.
[16] M. Nouri, B.K. Fussell, B.L. Ziniti, E. Linder, Real-time tool wear monitoring in milling using a cutting condition independent method, Int. J. Mach. Tools Manuf. 89 (2) (2014) 1–13.
[17] Z. Zhu, J. Sun, J. Li, P. Huang, Investigation on the influence of tool wear upon chip morphology in end milling titanium alloy Ti6Al4V, Int. J. Adv. Manuf. Technol. 83 (9) (2016) 1477–1485.
[18] E. Kuljanic, M. Sortino, TWEM, A method based on cutting forces-monitoring tool wear in face milling, Int. J. Mach. Tools Manuf. 45 (1) (2005) 29–34.
[19] S.N. Huang, K.K. Tan, Y.S. Wong, C.W.D. Silva, H.L. Goh, W.W. Tan, Tool wear detection and fault diagnosis based on cutting force monitoring, Int. J. Mach. Tools Manuf. 47 (3–4) (2007) 444–451.
[20] K. Zhu, T. Mei, D. Ye, Online condition monitoring in micromilling: a force waveform shape analysis approach, IEEE Trans. Ind. Electron. 62 (6) (2015) 3806–3813.
[21] Soichi Ibaraki, Takuya Shimizu, A long-term control scheme of cutting forces to regulate tool life in end milling processes, Precis. Eng. 34 (4) (2010) 675–682.
[22] H.R. Cao, X.W. Zhang, X.F. Chen, The concept and progress of intelligent spindles: a review, Int. J. Mach. Tools Manuf. 112 (2017) 21–52.
[23] Y. Altintas, Manufacturing Automation Metal Cutting Mechanics, Machine Tool Vibrations, and CNC Design, 2nd edition, Cambridge University Press, Cambridge, 2012, pp. 43–47.
[24] M. Wan, W.H. Zhang, G.H. Qin, G. Tan, Efficient calibration of instantaneous cutting force coefficients and runout parameters for general end mills, Int. J. Mach.

Tools Manuf. 47 (11) (2007) 1767–1776.
[25] Z. Zhu, R. Yan, F. Peng, X. Duan, L. Zhou, K. Song, C. Guo, Parametric chip thickness model based cutting forces estimation considering cutter runout of five-axis general end milling, Int. J. Mach. Tools Manuf. 101 (2) (2016) 35–51.
[26] C. Sun, Y. Altintas, Chatter free tool orientations in 5-axis ball-end milling, Int. J. Mach. Tools Manuf. 106 (7) (2016) 89–97.
[27] Z. Fu, W. Yang, X. Wang, J. Leopold, An analytical force model for ball-end milling based on a predictive machining theory considering cutter runout, Int. J. Adv. Manuf. Technol. 84 (9) (2016) 2449–2460.
[28] Y. Yang, W.H. Zhang, M. Wan, Effect of cutter runout on process geometry and forces in peripheral milling of curved surfaces with variable curvature, Int. J. Mach. Tools Manuf. 51 (5) (2011) 420–427.
[29] T.L. Schmitz, J. Couey, E. Marsh, N. Mauntler, D. Hughes, Runout effects in milling: surface finish, surface location error, and stability, Int. J. Mach. Tools Manuf. 47 (5) (2007) 841–851.
[30] K.X. Li, K.P. Zhu, T. Mei, A generic instantaneous undeformed chip thickness model for the cutting force modeling in micromilling, Int. J. Mach. Tools Manuf. 105 (6) (2016) 23–31.
[31] S.B. Wang, L. Geng, Y.F. Zhang, K. Liu, T.E. Ng, Cutting force prediction for five-axis ball-end milling considering cutter vibrations and run-out, Int. J. Mech. Sci. 96–97 (6) (2015) 206–215.
[32] E.M. Trent, P.K. Wright, Metal Cutting, 4th edition, Butterworth-Heinemann, Oxford, 2000, p. 54.
[33] M.C. Shaw, Metal Cutting Principles, 2nd edition, Oxford University Press, New York, USA, 2005, p. 176.
[34] E. Budak, Y. Altintas, E.J.A. Armarego, Prediction of milling force coefficients from orthogonal cutting data, J. Manuf. Sci. Eng. 118 (2) (1996) 216–224.
[35] M.H. DeGroot, Probability and Statistics, 2nd edition, Addison-Wesley Publishing Company, Boston, Massachusetts, USA, 1986.